Correlated substitution in paramagnetic Mn^{2+}-doped ZnO epitaxial films

T. C. Droubay,[1,*] D. J. Keavney,[2] T. C. Kaspar,[1] S. M. Heald,[2] C. M. Wang,[3] C. A. Johnson,[4] K. M. Whitaker,[4] D. R. Gamelin,[4] and S. A. Chambers[1]

[1]*Fundamental and Computational Sciences Directorate, Pacific Northwest National Laboratory, Richland, Washington 99352, USA*

[2]*Advanced Photon Source, Argonne National Laboratory, Argonne, Illinois 60439, USA*

[3]*Environmental Molecular Sciences Laboratory, Pacific Northwest National Laboratory, Richland, Washington 99352, USA*

[4]*Department of Chemistry, University of Washington, Seattle, Washington 98195, USA*

(Received 8 December 2008; revised manuscript received 26 February 2009; published 13 April 2009)

Epitaxial films of Mn^{2+}-doped ZnO were deposited by pulsed laser deposition on α-$Al_2O_3(0001)$ using targets created from Mn^{2+}-doped ZnO nanoparticles. Using x-ray absorption spectroscopy and x-ray magnetic circular dichroism, Mn(II) was found to substitute for Zn(II) in the würtzite ZnO lattice with only a paramagnetic dichroic component from the Mn and no magnetic component from either the O or Zn. The dichroism reveals that, while substitutional, the Mn^{2+} distribution in the ZnO lattice is not stochastic. Rather, Mn^{2+} has a tendency to substitute with higher effective local concentrations than anticipated from a stochastic doping model.

DOI: 10.1103/PhysRevB.79.155203 PACS number(s): 75.50.Pp, 81.15.Hi, 75.50.Gg, 75.25.+z

I. INTRODUCTION

ZnO, a wide band-gap semiconductor, has been extensively studied mainly due to its technological potential for UV optoelectronic applications.[1] ZnO has also been of interest because of predictions by Dietl *et al.*[2] and Sato and Katayama-Yoshida[3] of ferromagnetism in *p*-type Mn^{2+}:ZnO at temperatures above ambient. Using a mean-field approach, these authors predicted a hole-Mn^{2+} spin interaction of sufficient strength to render this material a candidate high-T_c diluted magnetic semiconductor (DMS). Since these predictions were made in 2000, there has been extensive research carried out on doping ZnO with not only Mn^{2+}, but with several other transition metals as well.[4,5] While ferromagnetism has been observed in some of these materials, consensus has not been reached as to the physical cause of the ferromagnetism and debate continues in the literature as to whether the ferromagnetism is intrinsic at all or instead results from magnetic precipitates, contamination, or otherwise hidden ferromagnetic secondary phases.[6–9]

Both the theoretical work of Dietl and co-workers[2,10] and *ab initio* calculations by Sato and Katayama-Yoshida[11] suggest that robust room-temperature ferromagnetism will occur through carrier-mediated exchange in Mn^{2+}:ZnO, but only for *p*-type material. If electrons are introduced rather than holes, antiparallel spin coupling is favored over parallel spin alignment. An exceedingly wide range of experimental results has been reported, ranging from intrinsic room-temperature ferromagnetic ordering[5,12–20] to nonferromagnetic (paramagnetic or antiferromagnetic) (Refs. 21–28) or spin-glass behavior.[29–31] Despite the fact that Mn has a high solubility in ZnO (Ref. 32) and the most likely secondary phases (Mn metal, MnO, Mn_2O_3, MnO_2, and Mn_3O_4) are either antiferromagnetic or ferromagnetic with a low Curie temperature ($\sim$40 K),[33] several groups have reported extrinsic sources of room-temperature ferromagnetism in Mn:ZnO.[34–40] The solid solubility of Mn^{2+} in ZnO exceeds 15% (cation percent) under typical growth conditions.[41,42] While not all studies agree on the identity of the ferromagnetic secondary phase, most suggest a metastable ferromagnetic phase, $Mn_{2-x}Zn_xO_{3-\delta}$, formed by Zn^{2+} diffusion into Mn^{3+} oxide (Mn_2O_3) during low to modest temperature processing as originally proposed by Kundaliya *et al.*[37] These authors deduce that heating this metastable phase to temperatures above the nominal Curie temperature ($\sim$980 K) eliminates the ferromagnetic ordering by phase transformation. In light of the possibility of extrinsic ferromagnetism due to magnetic contamination[9] or secondary phase formation,[8,34–39] the need for definitive materials characterization is clear.

Other literature points to the possibility that Mn-doped ZnO shows intrinsic DMS ferromagnetism when doped *p* type. In experimental studies of polycrystalline Mn^{2+}:ZnO films prepared by spin-coat processing of colloidal Mn^{2+}:ZnO nanocrystals,[20,43,44] experimental trends were found that agreed with many of the theoretical predictions[2,10,11,45,46] with respect to the influence of added nitrogen. Using a chemical approach that allowed the introduction of nitrogen, a *p*-type dopant in ZnO, these authors showed that N-doped Mn^{2+}:ZnO displayed strong ferromagnetism even when starting with 0.2% Mn^{2+}:ZnO colloidal nanocrystals and using conditions where there is insufficient Mn^{2+} mobility to form enriched phases such as $Mn_{2-x}Zn_xO_{3-\delta}$. Polycrystalline films made from the same colloidal Mn^{2+}:ZnO nanocrystals without addition of a nitrogen source were paramagnetic. Similar trends have been reported for Mn:ZnO thin films codoped with N for *p*-type conductivity.[47–49]

The lack of consensus and the claims of extrinsic ferromagnetism arising from ferromagnetic precipitates or secondary phases demonstrate the need for discriminating materials characterization and magnetic measurements that can distinguish between intrinsic and extrinsic sources of the ferromagnetism. In this work, we have used such probes to investigate Mn^{2+}:ZnO epitaxial films grown by pulsed laser deposition (PLD). We have made our PLD targets with colloidal Mn^{2+}:ZnO nanoparticles rather than mixed ZnO and Mn oxide powder as is typical. Previous work indicated that starting target materials that are compositionally uniform on

the nanoscale may ablate more congruently than materials that are heterogeneous over ~ 1 μm length scale.[50] We have compared the properties of epitaxial $Mn_xZn_{1-x}O$ films and the Mn^{2+}:ZnO nanoparticles from which the PLD targets were made. Both the epitaxial films and nanoparticles were found to be of very high structural quality. The magnetic properties of these films were investigated for a range of Mn concentrations by x-ray magnetic circular dichroism (XMCD), which provides atom-specific information for each species in the lattice.

II. EXPERIMENT

Pulsed laser deposition was used to deposit epitaxial thin films of $Mn_xZn_{1-x}O$ onto α-$Al_2O_3(0001)$ (*c*-plane sapphire) substrates. In order to eliminate the deposition of molten droplets or constituent phase particles onto the substrate during the laser ablation process, an off-axis growth configuration[51] and nanoparticle targets are used. The laser spot from a KrF laser (248 nm) was rastered across a rotating target while the substrate was also rotating, allowing for uniform deposition across the substrate. Several separate targets were used in this study, depending upon the desired dopant(s) and concentration(s). These include $Mn_{0.05}Zn_{0.95}O$ nanoparticles, $Mn_{0.002}Zn_{0.998}O$ nanoparticles, pure (99.999%) ZnO powder, and combustion-synthesized[52] Al-doped ZnO nanoparticles. Each starting material was mixed with small amounts of deionized water and polyethylene glycol binder, cold pressed, and sintered for 8 h at ~ 1000 °C in O_2. To remove any residual surface contamination, the targets were ablated in 10 mTorr of O_2 prior to every deposition. Carbon is predicted by Pan *et al.*[53] to be an electronic and magnetic dopant within ZnO. X-ray photoemission spectroscopy (XPS) and the high resistivity of undoped ZnO confirm the lack of carbon within the films. When a stoichiometry other than that of the targets was sought, the film composition was varied by combining laser pulses from the different targets in various proportions under computer control. In a typical two-target growth, a few laser pulses would be incident on one target. The laser shutter would then be closed and a second target would be moved into position, followed by reopening of the shutter and laser pulses directed onto the second target. The process would then be repeated as many times as necessary to achieve the desired film thickness. Films with dopant concentrations of up to 5% were routinely grown in this way.

The $Mn_xZn_{1-x}O$ nanocrystalline target materials were synthesized at room temperature by addition of 1.7 equivalents of an ethanolic solution of 0.55 M tetramethylammonium hydroxide $[N(Me)_4OH \cdot 5H_2O]$ to a 0.10 M solution of $x Mn(OAc)_2 \cdot 4H_2O/(1-x)Zn(OAc)_2 \cdot 2H_2O$ dissolved in ethanol under constant stirring.[54] Excess reactants were removed from the nanocrystals by iterative washing and resuspension in heptanes and ethanol, respectively. The nanocrystals were then calcined at 550 °C for 1–2 h and ground into a fine powder. Detailed description of the synthesis and characterization of colloidal Mn^{2+}:ZnO quantum dots can be found elsewhere.[54]

Double-sided epipolished $10 \times 5 \times 0.5$ mm^3 α-$Al_2O_3(0001)$ substrates from Crystec were used for all growths. To ensure that the substrates were free from ferromagnetic contamination, each substrate was screened prior to growth with vibrating sample magnetometry (VSM) at room temperature. If the substrates exhibited ferromagnetism, the back and edges would be selectively etched in concentrated HNO_3 and rechecked with VSM.[55] The substrates were ultrasonically washed in methanol and isopropanol before introduction into the vacuum chamber. After sample introduction and prior to growth, the substrates were heated up to 550 °C in 10 mTorr O_2 to eliminate adventitious carbon from the growth surface.

All $Mn_xZn_{1-x}O$ film growths were carried out in 10 mTorr O_2 and at a substrate temperature of 550 °C. The single target $Mn_{0.05}Zn_{0.95}O$ films were grown at a laser repetition rate of 1–5 Hz, the mixed-target $Mn_{0.025}Zn_{0.975}O$ films were grown at 2 Hz, and the $Mn_{0.002}Zn_{0.998}O$ film was grown at 10 Hz. No significant differences in structural quality or Mn incorporation were observed in films deposited at different laser repetition rates (≤ 10 Hz) or for different film thicknesses which ranged from 50–1000 nm. The $Mn_{0.05}Zn_{0.95}O$ and $Mn_{0.002}Zn_{0.998}O$ films were grown using single targets whereas the $Mn_{0.025}Zn_{0.975}O$ films were grown by toggling between the $Mn_{0.05}Zn_{0.95}O$ and pure ZnO target, as described above. To investigate the influence of donors on the magnetic properties of Mn^{2+}:ZnO films, (Mn,Al) codoped ZnO films were grown by toggling between the $Mn_{0.05}Zn_{0.95}O$ and $Al_{0.01}Zn_{0.99}O$ targets.

The whole-sample magnetic properties of the films were measured at room temperature by VSM with the magnetic field applied in the plane of the film. High-resolution x-ray diffraction (HRXRD) and high-resolution transmission electron microscopy (TEM) were used to investigate the crystallinity and detailed microstructure of the films. A four-point probe in linear geometry was used to determine room-temperature resistivities. XPS was performed in a Gammadata/Scienta SES 200 photoelectron spectrometer with monochromatic Al-$K\alpha$ x-ray source.

X-ray absorption near-edge spectroscopy (XANES) and extended x-ray absorption fine structure (EXAFS) were performed on the PNC-CAT bending magnet (20-BM) and insertion device (20-ID) beamlines at the Advanced Photon Source located at Argonne National Laboratory. The *K*-edge XANES and EXAFS in fluorescence mode are sensitive probes of the Mn dopant valence state and lattice location. Sample rotation about the surface normal was used to minimize Bragg diffraction effects and spectra collected with crossed (perpendicular and parallel) polarizations, relative to the sample surface, were appropriately averaged such that the XANES and EXAFS of the epitaxial films could be directly compared to those measured for the Mn^{2+}:ZnO nanoparticles and pure ZnO powder standard. *L*-edge XANES and XMCD were also performed at the Advanced Photon Source using beamline 4-ID-C to probe the spin dependent densities of states associated with Mn, Zn, and O. The samples were placed on a split-coil superconducting solenoid mounted on a liquid He cryostat with the magnetic field parallel to the beam propagation direction (Faraday geometry) and with a $\sim 10°$ incident angle with respect to the plane of the film. Circularly polarized x-rays were generated using a helical undulator. XANES scans were taken down to 4.2 K in

fields up to 5 T in total fluorescence yield (TFY) using a Ge solid-state detector. The dichroism spectra were generated by reversing the polarization of the incident x-rays at each energy point of the XANES spectra (TFY) for better background matching. For clarity, the XMCD or dichroism signal is defined as $\sigma_{XMCD}=(\sigma^+-\sigma^-)$, where σ^+ (σ^-) is the TFY intensity measured using right (left) circularly polarized photons, defined as viewed from source to detector. The normalization procedure, described in detail later, compensates for the total amount of Mn atoms such that a comparison can be made between samples and doping levels, i.e., $\sigma_{Mn}=(\sigma^+-\sigma^-)/(\sigma_{L_3})$.

III. RESULTS

A. Film crystallinity and microstructure

Under the deposition conditions of 10 mTorr O_2 and 550 °C, epitaxial films with good crystallinity and a sharp interface were deposited on *c*-plane sapphire substrates. XRD (not shown) reveals (0001) oriented films with good crystallinity and little mosaic spread. Pole figures for pure ZnO grown by PLD under similar conditions confirm a 30° rotation of the ZnO *a* axis relative to that of the substrate.[51] Glancing-incidence measurements, which exhibit enhanced sensitivity to the film, do not reveal any secondary phases. Moreover, the lattice parameters remain unchanged within experimental error as the Mn concentration increases from $x=0$ to $x=0.05$ despite clear evidence from XANES and EXAFS that Mn^{2+} substitutes for Zn^{2+} as discussed below. Other mechanisms which induce strain in Mn^{2+}:ZnO (such as lattice mismatch) or reduce strain (such as misfit dislocations) dominate over Mn^{2+} incorporation in dictating the lattice parameters in the epitaxial films, especially considering the relatively low Mn^{2+} concentrations used. The TEM micrographs shown in Fig. 1 reveal a smooth epitaxial film comprised of columnar grains with sharp interfaces to the substrate. The diameters of the columnar grains range from ~20 to >150 nm, with an average diameter of ~75 nm, as judged by several low-magnification images. Selected-area diffraction patterns (not shown) from adjacent oriented columnar grains reveal a slight in-plane rotation of ~1°–2°. The columnar growth and in-plane rotational variation of the grains is presumably a result of the 18% lattice mismatch between ZnO(0001) and α-Al_2O_3(0001). The interface between the sapphire substrate and the Mn^{2+}:ZnO film [Fig. 1(c)] within each grain is sharp as a result of domain matching epitaxy,[56] with little evidence of interdiffusion between the ZnO and Al_2O_3. No evidence of Mn segregation or secondary phases was found in $Mn_{0.05}Zn_{0.95}O$ films grown by PLD.

B. Mn charge state and local structure

The insensitivity of laboratory-based XRD and the small volume sampled by TEM make these probes inadequate for comprehensive secondary phase detection. In contrast, spectroscopic techniques such as x-ray absorption in fluorescence detection mode are more effective because these methods are element specific and probe the entire film depth. Mn and Zn *K*-edge XANES and EXAFS were used to investigate the dopant speciation, probe for secondary phases, and provide information on the detailed structural environment of the Mn dopants. Mn *K*-edge XANES spectra are shown in Fig. 2 for a PLD grown $Mn_{0.05}Zn_{0.95}O/Al_2O_3$(0001) film along with the Mn^{2+}:ZnO nanoparticle target material. The similarity of the Mn *K*-edge XANES energy positions and line shapes for the Mn^{2+}:ZnO film and Mn^{2+}:ZnO nanoparticles indicates that neither the oxidation state nor the local environment of the Mn ions changes appreciably during the laser ablation process. Moreover, the location and shape of the Mn pre-edge feature at ~6539 eV are identical for the nanoparticle target material and the PLD-grown film, further corroborating that the formal oxidation state of the Mn ions does not change as a result of the ablation process.

Figure 2 also contains Mn *K*-edge XANES from reference standards of Mn metal, Mn^{2+} (rhodochrosite), Mn^{3+} (Mn ferrite), and Mn^{4+} (todorokite). Based on overall shape and the Mn absorption edge inflection point, the presence of minority species containing Mn(0) and Mn(IV) in the films and nanoparticles can be eliminated. However, lacking a tetrahedrally coordinated Mn oxide standard with one pure valence state, it was not possible to discriminate between Mn(II) and Mn(III) in the films based on edge position, as discussed by Farges.[57] This was particularly true for Mn(II) compounds, in which the edge position varied by as much as 6 eV. However, previous work by Titov *et al.*[58] using Mn XANES in (Ga,Mn)N showed that the pre-edge peak is sensitive to the Mn charge state in tetrahedrally coordinated Mn compounds. A single pre-edge absorption peak indicates $d^5(Mn^{2+})$, as seen in the Mn XANES of (Zn,Mn)Te, whereas a double peaked pre-edge structure indicates $d^4(Mn^{3+})$.[58] The single Mn pre-edge absorption peak observed here allows us to unequivocally assign the formal oxidation state in both the Mn^{2+}:ZnO nanoparticles and Mn^{2+}:ZnO PLD films as +2. This distinct pre-edge feature also indicates that Mn(II) ions are tetrahedrally coordinated within the material because the pre-edge features in octahedrally coordinated Mn(II) compounds are weak or nonexistent due to parity selection rules.

Figure 3 shows the Fourier transforms of the Mn *K*-shell EXAFS for a representative PLD grown Mn:ZnO film (red dotted line), the Mn:ZnO nanoparticles (blue dashed-dot), and the Zn *K*-shell EXAFS of ZnO powder (solid black line). Comparison of the spectra confirms that Mn has substituted for Zn within the ZnO lattice in both the colloidal Mn^{2+}:ZnO nanoparticles and the Mn^{2+}:ZnO/Al_2O_3(0001) epitaxial film. The Mn-O bonds are about 0.05 Å longer than the Zn-O bonds in ZnO. This is consistent with the ionic radii of fourfold coordinated Mn^{2+} (0.66 Å) and Zn^{2+} (0.60 Å),[59] which gives further confirmation of Mn^{2+} substitution. The small differences that arise between the film(s) and the nanoparticles most likely result from the single crystalline orientation of the epitaxial films. The EXAFS measurements provide further evidence that there is no secondary phase formation in either the Mn^{2+}:ZnO thin films or the Mn^{2+}:ZnO nanoparticles. These data support previous findings that Mn substitutes for Zn in Mn^{2+}:ZnO nanoparticles obtained from a combination of electron-paramagnetic resonance, optical magnetic circular dichroism (MCD), electronic absorption, and magnetic-susceptibility data.[20,43,44,54]

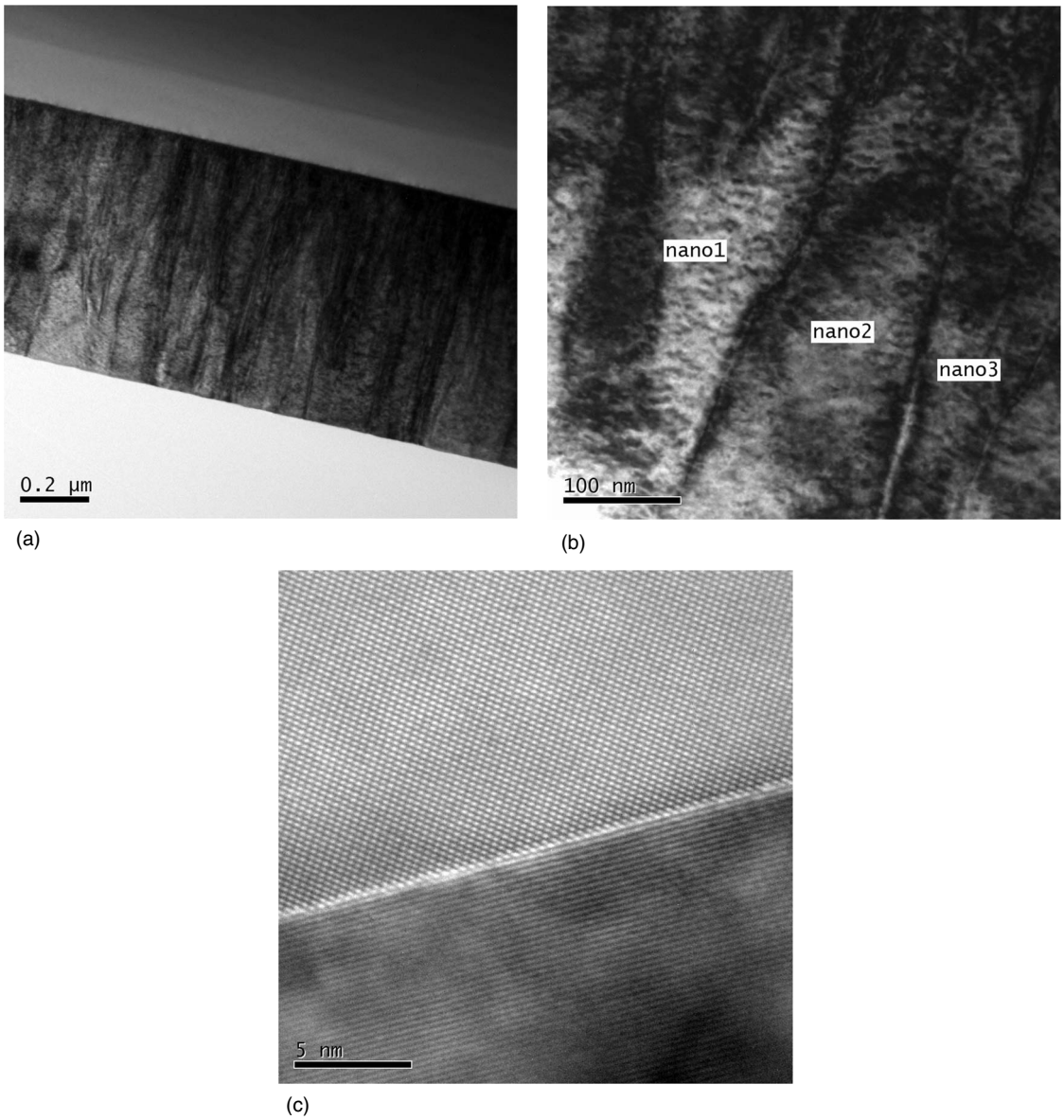

FIG. 1. TEM of $Mn_{0.05}Zn_{0.95}O/Al_2O_3(0001)$ deposited from colloidal Mn^{2+}:ZnO nanoparticle target. (a) Low magnification micrograph showing a smooth film comprised of (b) columnar grains labeled nano1, nano2, and nano3. (c) High-resolution micrograph of $Mn_{0.05}Zn_{0.95}O/Al_2O_3$ interface.

C. Magnetic measurements

The resistivity of $Mn_{0.05}Zn_{0.95}O$ films grown by PLD in 10 mTorr of O_2 is typically $>10^4$ Ω cm. As mentioned previously, Mn^{2+}:ZnO is predicted to be ferromagnetic when doped *p* type. As a general rule, *n*-type doping of ZnO is relatively easy whereas *p*-type doping has proven to be much more difficult. In order to investigate the ferromagnetic behavior of Mn^{2+}:ZnO films in both regimes, Mn^{2+}:ZnO films were codoped with Al for *n*-type conduction and grown in 10 mTorr of N_2 or N_2O within the PLD system to attempt *p*-type doping. Neither of these doping schemes has a measurable effect on the Mn *K*-shell XANES and EXAFS, revealing that Mn dopants remain in the +2 formal charge state and at Zn sites, with no evidence of secondary phase formation. Doping with Al reduces the resistivity of the films by several orders of magnitude. Preliminary results provide no evidence of N incorporation or *p*-type conductivity for films deposited in N_2 or N_2O. Moreover, films at all dopant levels and resistivities remain paramagnetic at room temperature as measured by VSM.

Low signals from dilute dopants, riding atop a paramagnetic/diamagnetic background from the host and substrate, present an inherent difficulty in attributing any observed ferromagnetism to either intrinsic or extrinsic origins from whole-sample magnetization measurements. The elemental and chemical specificities of x-ray absorption and XMCD, however, provide a sound test of the origin of the individual spin polarization and whether it is consistent with the bulk magnetization.

Figure 4(a) shows the in-plane Mn L_3 absorption (TFY) and dichroism in a magnetic field for films with different Mn

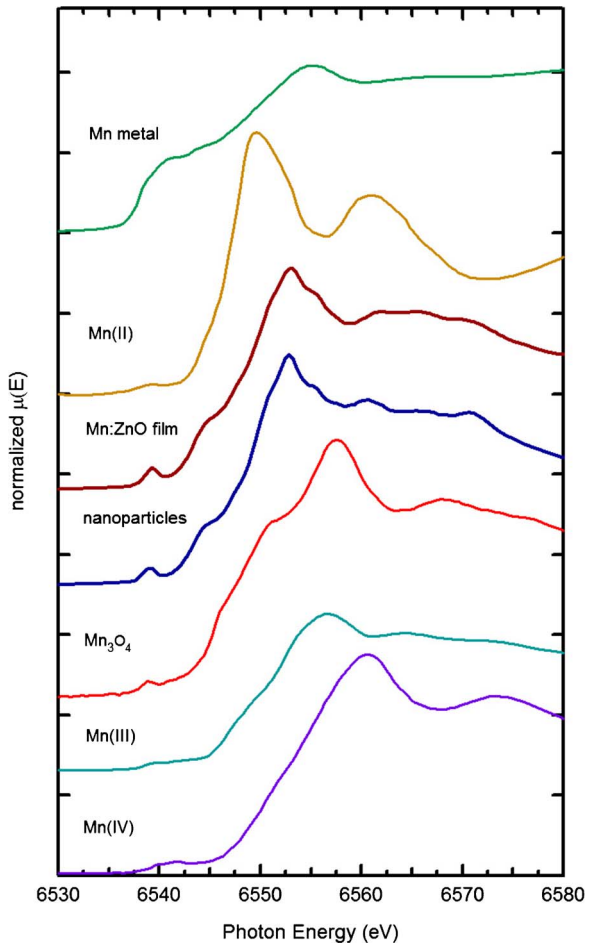

FIG. 2. (Color online) Mn *K*-shell XANES showing similarity between representative PLD grown Mn:ZnO film (thick red) and Mn:ZnO nanoparticles (thick blue) along with Mn standards. Near-edge spectra from bottom to top are todorokite $[(Mn,Mg,Ca,Ba,K,Na)_2Mn_3O_{12}\cdot 3H_2O]$, Mn ferrite ($MnFe_2O_4$), Mn:ZnO nanoparticles, Mn:ZnO film, rhodochrosite ($MnCO_3$), and Mn metal. Curves have been offset for clarity.

concentrations measured at 4 K. The x-ray absorption spectra have been normalized on a per-Mn basis such that the edge jump is unity. The three L_3 features at 635, 636.5, and 638.6 eV are present in all samples and are consistent with Mn(II) in a tetrahedral environment.[60] A small shoulder or peak on the lower energy side of the L_3 peak maximum (~634.5 eV) can also be seen in the more heavily doped samples, which is also consistent with tetrahedral Mn(II). The small signal-to-noise ratio in the measurements for the lower Mn^{2+} concentrations prevents clear identification of this feature at 634.5 eV. It should be noted that these measurements were taken in the more bulk-sensitive but less efficient TFY mode in order to probe the Mn throughout the film, rather than the more surface-sensitive total electron yield (TEY) mode. TEY data were also collected, but charging of the samples due to their high resistivity precluded getting good data. At in-plane magnetic field values of 5 T and a temperature of 5 K, the dichroism for the three main features is clearly seen at all three concentrations.

Figure 4(b) shows Mn L_3 x-ray absorption and XMCD spectra for the 5% Mn^{2+}-doped ZnO film collected at 5 K as

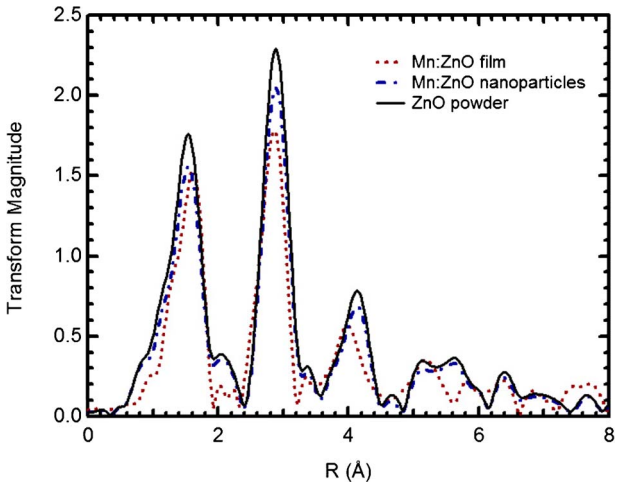

FIG. 3. (Color online) Fourier transform of the Mn *K*-shell EXAFS of a PLD grown $Mn_{0.05}Zn_{0.95}O$ film (red dotted), $Mn_{0.05}Zn_{0.95}O$ nanoparticles (blue dashed-dot), and the Zn *K*-shell EXAFS of ZnO powder showing substantial Mn substitution within the ZnO lattice.

a function of magnetic field. As the strength of the magnetic field increases from 0 to 5 T the dichroism magnitude also increases. The absence of circular dichroism at zero field indicates that the sample is either paramagnetic, superparamagnetic, or a soft ferromagnet with little remanence at 5 K. The field dependence of the XMCD is similar for all three concentrations, establishing that the Mn^{2+} ions within the $Mn_xZn_{1-x}O$ films are paramagnetic. The lack of a blocking temperature or critical point in the Curie-like temperature dependence of the Mn XMCD intensity (Fig. 5) rules out superparamagnetism or spin-glass behavior in all films examined. Both the O *K* and Zn *L* edges were investigated to check for spin polarization on the O and Zn atoms in the 5% Mn:ZnO film. No XMCD signal was seen for either element at fields up to 5 T.

The Mn^{2+} XMCD intensities are expressed using a relative scale as follows. First, the Mn L_3 XMCD peak area after linear background subtraction was divided by the total area under the L_3 XAS peak to eliminate the Mn^{2+} concentration dependence. Second, the dichroism per Mn^{2+} was normalized by defining a maximum magnetic moment per dopant of unity at 5 K and at a field of 5 T in the dilute limit. By dilute limit we mean Mn concentrations sufficiently low such that 100% of the dopants are mutually isolated (i.e., have no other dopants in the adjacent cation coordination sphere). The experimental data for the most dilute sample examined here ($Mn_{0.002}Zn_{0.998}O$) were then fit to a Brillouin function with $J=5/2$ and were scaled such that the dichroism from the Brillouin function is ~0.98 at 5K in a field of 5 T. The rationale for the value 0.98 is given in Sec. III. Data for $Mn_{0.025}Zn_{0.975}O$ and $Mn_{0.05}Zn_{0.95}O$ were analyzed in the same way and fits to Brillouin functions ($J=5/2$, $g=1.998$, $T=5$ K) were carried out. The results are shown in Fig. 6, with the Brillouin functions shown as solid curves.

The statistical probability of forming dopant pairs and clusters that align antiferromagnetically implies that the apparent magnetic moment per Mn^{2+} will decrease as the Mn^{2+}

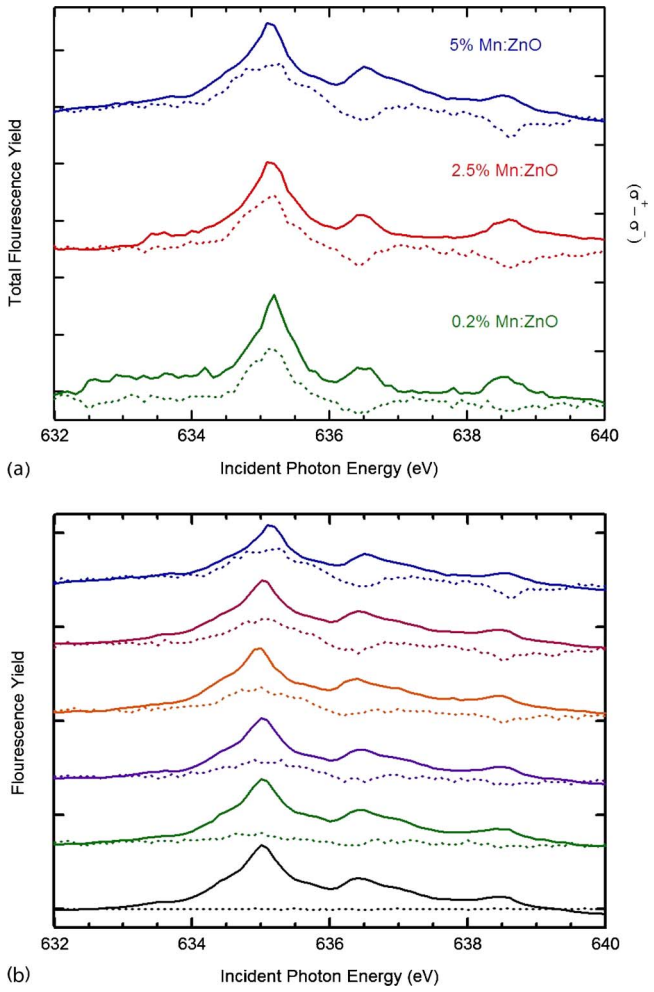

FIG. 4. (Color online) (a) Low-temperature in-field x-ray absorption (solid) and dichroism (dashed) at the Mn L_3 edge for $Mn_{0.05}Zn_{0.95}O$ (blue), $Mn_{0.025}Zn_{0.975}O$ (red), and $Mn_{0.002}Zn_{0.998}O$ (green) at 5 Tesla. (b) Low-temperature x-ray absorption (solid) and dichroism (dashed) for 5% Mn-doped ZnO film. The in-plane magnetic field values range from 0 T (bottom) to 5 T (top) in steps of 1 T. The dichroism spectra have been scaled by a factor of 10 with respect to the x-ray absorption spectra.

concentration increases. Significantly, the normalized moment from the Brillouin fits to the data decreases from 0.98 for $Mn_{0.002}Zn_{0.998}O$ to 0.53 for $Mn_{0.025}Zn_{0.975}O$ and to ~0.26 for $Mn_{0.05}Zn_{0.95}O$. As discussed in detail below, this rate of falloff in the normalized Mn moment with increasing concentration is substantially higher than expected based on probability predictions[61,62] of dopant cluster formation in which a stochastic dopant distribution is assumed.

IV. DISCUSSION

Pairs of dopants separated by an intervening oxygen atom usually couple antiferromagnetically due to superexchange in both the würtzite and zinc-blende structures.[63,64] For nearest-neighbor cations in Mn^{2+}:ZnO, the values for the two largest exchange constants have been experimentally determined to favor antiparallel alignment

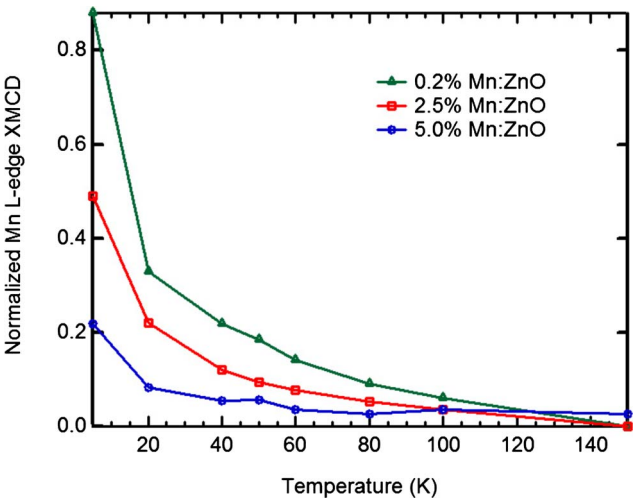

FIG. 5. (Color online) Temperature dependence of the maximum of the Mn L_3 dichroism on a per-Mn basis for the 0.2% Mn:ZnO (triangles), 2.5% Mn:ZnO (squares), and 5% Mn:ZnO (circles) thin films. Lines are drawn to guide the eyes.

(antiferromagnetic).[65,66] Interestingly, however, the simulations performed by Gratens *et al.*[65] to determine the exchange constants assumed a random Mn^{2+} distribution. The normalized magnetic moment per dopant depends on the population distribution for the various dopant cluster sizes and bonding configurations.[62,67] In order to treat the problem quantitatively, we describe dopant clusters in terms of an "*n*-mer," which is defined as *n* dopant cations directly connected through intervening oxygen atoms in a würtzite cluster. In this approach, we define the normalized total magnetic moment of an isolated dopant atom to be unity. Due to superexchange, pairs of dopant atoms couple antiferromagnetically, resulting in a normalized moment of zero for all *n*-mers with even *n*. Trimers and all higher-order odd *n*-mers are approximated to yield a normalized magnetic moment per dopant of $1/n$. In these dilute systems where superex-

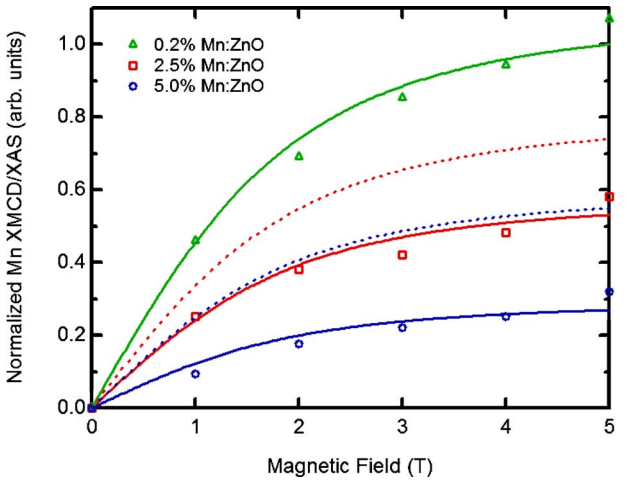

FIG. 6. (Color online) Brillouin fits (solid) and expected normalized Mn magnetization (dashed) assuming stochastic distribution of Mn ions for $Mn_{0.002}Zn_{0.998}O$ (green triangles), $Mn_{0.025}Zn_{0.975}O$ (red squares), and $Mn_{0.05}Zn_{0.95}O$ (blue circles).

change is the dominant short-range interaction, the magnetic moment is dominated by isolated dopants and trimers. For simplicity, we neglect the contributions of closed trimers and other "frustrated spin" bonding configurations for which this even/odd *n*-mer generalization does not hold. For the Mn concentrations experimentally explored, these configurations occur relatively infrequently. Thus, the anticipated error resulting from their neglect is small.

We have shown elsewhere that the dopant distribution in structures with a high surface-to-volume ratio can deviate significantly from the predictions of probabilistic expressions for infinite bulk lattices and higher dopant concentrations.[62] Our Monte Carlo (MC) simulations for cation doping of ZnO at $x=0.002$ agree with the predictions of Behringer[61] which are based on infinite bulk lattices and show that at $x=0.002$ approximately 98% of the dopants are isolated and the remainder are dimers. Hence, the normalized magnetic moment per Mn^{2+} should be ~0.98 at $x=0.002$. However, the same MC simulations for model grain shapes like those seen in TEM micrographs (Fig. 1) predict a moment per Mn^{2+} that is greater than the bulk-lattice prediction for $x=0.025$ and 0.05 due to the finite surface-to-volume ratio of the columnar grains.

Using dopant distributions from our MC simulations, the field dependence of the expected average magnetic moment per dopant is plotted for the higher Mn^{2+} concentrations as dashed lines in Fig. 6. The expected moments derived from the MC simulations differ significantly from the measured values. The normalized moments per Mn^{2+} from MC are ~0.74 for $Mn_{0.025}Zn_{0.975}O$ and ~0.55 for $Mn_{0.05}Zn_{0.95}O$ at 5 K and a field of 5 T compared to 0.53 and 0.26 from experiment, respectively. These differences in moment per Mn^{2+} between experiment and MC predictions at $x=0.025$ and 0.05 reveal that the Mn^{2+} dopants are not stochastically distributed throughout the lattice, but rather tend to cluster together. This clustering does not imply secondary phase formation nor does it represent material decomposition. Rather, the Mn^{2+} concentration varies from one volume element to another although all Mn^{2+} dopants are located at würtzite cation sites. This process, which might be described as correlated substitution,[68] is presumably driven by a lowering of the total free energy driven by smaller Mn-Mn separations in the lattice. This correlated substitution of Mn^{2+} in $Mn_xZn_{1-x}O$ epitaxial films does not result in ferromagnetic interaction in semi-insulating or *n*-type material. Based on comparison of the normalized XMCD field dependence with the MC simulations, the effective Mn^{2+} concentrations (x_{loc}) are 0.002, 0.044, and 0.22 for the $x=0.002$, 0.025, and 0.05 samples, respectively.

Clustering of dopants into regions of high local dopant concentration does not preclude the material from being a useful DMS. Various groups have argued that ferromagnetic semiconductors with Curie temperatures well-above room temperature may in fact result from structures characterized by correlated substitution or spinodal decomposition.[6,13,68–71] However, White *et al.*[72] found that neither correlated substitution nor spinodal decomposition in würtzite $Co_xZn_{1-x}O$ nanoparticles results in ferromagnetism in that DMS. This finding implies that structural imperfections such as grain boundaries or other defects may be crucial, a conclusion drawn previously from various oxide DMS microstructure/magnetism correlations.[55,73–78] These structural imperfections may lead to increased dopant mobility within the lattice, to carrier introduction, to polaron stabilization through carrier binding, or to the introduction of some other ferromagnetic coupling mechanisms. The results clearly show that structurally excellent Mn^{2+}-doped ZnO thin films are paramagnetic, at least in the absence of a high concentration of holes from a secondary dopant such as N. The absence of intrinsic ferromagnetism is in agreement with previous results for structurally excellent Co^{2+}-doped TiO_2 anatase,[79] Cr^{3+}-doped TiO_2 anatase,[73] and Co^{2+}-doped ZnO[80] thin films.

V. CONCLUSION

Epitaxial films of Mn^{2+}-doped ZnO were grown on *c*-sapphire substrates by off-axis PLD using targets made from Mn^{2+}:ZnO nanoparticles. The resultant epitaxial films were of high structural quality, possessed volume-averaged Mn/Zn ratios that were close to those of the PLD target materials, and had no detectable Mn-containing secondary phases or precipitates. The Mn(II) dopants were found to substitute for Zn in the würtzite ZnO lattice. All films were paramagnetic with the measured magnetic moment associated exclusively with Mn^{2+}; no paramagnetism was detected by either Zn or O *L*-edge XMCD. The substitutional Mn^{2+} ions showed a propensity to cluster, yielding higher effective concentrations than anticipated from the volume-averaged Mn/Zn ratios. The correlated substitution revealed by x-ray absorption spectroscopy is not detected in the TEM micrographs. It remains to be determined if such correlated substitution is advantageous in stabilizing a ferromagnetic ground state for *p*-type Mn^{2+}:ZnO films.

ACKNOWLEDGMENTS

A portion of the research was performed using EMSL, a national scientific user facility sponsored by the Department of Energy's Office of Biological and Environmental Research located at Pacific Northwest National Laboratory. This work was supported by the U.S. Department of Energy, Office of Science, Office of Basic Energy Sciences, Division of Materials Science and Engineering Physics. The UW-PNNL collaboration is sponsored by the NSF (Contract No. CRC-0628252). Additional support to D.G. from the Sloan Foundation, the Dreyfus Foundation, and the Research Corporation is gratefully acknowledged. Use of the Advanced Photon Source at Argonne National Laboratory was supported by the U.S. Department of Energy, Office of Science, Office of Basic Energy Sciences under Contract No. DE-AC02-06CH11357.

*Corresponding author; PNNL, PO 999, MSIN K8-87, Richland, WA 99352; FAX: (509)371-6242; tim.droubay@pnl.gov

[1] Ü. Özgür, Ya. I. Alivov, C. Liu, A. Teke, M. A. Reshchikov, S. Doğan, V. Avrutin, S.-J. Cho, and H. Morkoç, J. Appl. Phys. **98**, 041301 (2005).
[2] T. Dietl, H. Ohno, F. Matsukura, J. Cibert, and D. Ferrand, Science **287**, 1019 (2000).
[3] K. Sato and H. Katayama-Yoshida, Jpn. J. Appl. Phys., Part 2 **39**, L555 (2000).
[4] S. J. Pearton, W. H. Heo, M. Ivill, D. P. Norton, and T. Steiner, Semicond. Sci. Technol. **19**, R59 (2004).
[5] F. Pan, C. Song, X. J. Liu, Y. C. Yang, and F. Zeng, Mater. Sci. Technol. **62**, 1 (2008).
[6] T. Dietl, J. Phys.: Condens. Matter **19**, 165204 (2007).
[7] T. Fukumura, H. Toyosaki, and Y. Yamada, Semicond. Sci. Technol. **20**, S103 (2005).
[8] T. C. Kaspar, T. Droubay, S. M. Heald, M. H. Engelhard, P. Nachimuthu, and S. A. Chambers, Phys. Rev. B **77**, 201303(R) (2008).
[9] S. A. Chambers, Surf. Sci. Rep. **61**, 345 (2006).
[10] T. Dietl, H. Ohno, and F. Matsukura, Phys. Rev. B **63**, 195205 (2001).
[11] K. Sato and H. Katayama-Yoshida, Semicond. Sci. Technol. **17**, 367 (2002).
[12] P. Sharma, A. Gupta, K. V. Rao, F. J. Owens, R. Sharma, R. Ahuja, J. M. O. Guillen, B. Johansson, and G. A. Gehring, Nature Mater. **2**, 673 (2003).
[13] H. Katayama-Yoshida, K. Sato, T. Fukushima, M. Toyoda, H. Kizaki, V. A. Dinh, and P. H. Dederichs, J. Magn. Magn. Mater. **310**, 2070 (2007).
[14] W. Y. Shim, K. A. Jeon, K. I. Lee, S. Y. Lee, M. H. Jung, and W. Y. Lee, J. Electron. Mater. **35**, 635 (2006).
[15] H. Schmidt, M. Diaconu, H. Hochmuth, M. Lorenz, A. Setzer, P. Esquinazi, A. Pöppl, D. Spemann, K.-W. Nielsen, R. Gross, G. Wagner, and M. Grundmann, Superlattices Microstruct. **39**, 334 (2006).
[16] N. Theodoropoulou, V. Misra, J. Philip, P. LeClair, G. P. Berera, J. S. Moodera, B. Satpati, and T. Som, J. Magn. Magn. Mater. **300**, 407 (2006).
[17] H. Y. Xu, Y. C. Liu, C. S. Xu, Y. X. Liu, C. L. Shao, and R. Mu, J. Chem. Phys. **124**, 074707 (2006).
[18] D. P. Norton, S. J. Pearton, A. F. Hebard, N. Theodoropoulou, L. A. Boatner, and R. G. Wilson, Appl. Phys. Lett. **82**, 239 (2003).
[19] N. A. Theodoropoulou, A. F. Hebard, D. P. Norton, J. D. Budai, L. A. Boatner, J. S. Lee, Z. G. Khim, Y. D. Park, M. E. Overberg, S. J. Pearton, and R. G. Wilson, Solid-State Electron. **47**, 2231 (2003).
[20] K. R. Kittilstved, W. K. Liu, and D. R. Gamelin, Nature Mater. **5**, 291 (2006).
[21] E. Chikoidze, Y. Dumont, H. J. von Bardeleben, J. Gleize, F. Jomard, E. Rzepka, G. Berrerar, D. Ferrand, and O. Gorochov, Appl. Phys. A: Mater. Sci. Process. **88**, 167 (2007).
[22] X. M. Cheng and C. L. Chien, J. Appl. Phys. **93**, 7876 (2003).
[23] S. Kolesnik and B. Dabrowski, J. Appl. Phys. **96**, 5379 (2004).
[24] S. J. Han, T. H. Jang, Y. B. Kim, B. G. Park, J. H. Park, and Y. H. Jeong, Appl. Phys. Lett. **83**, 920 (2003).
[25] S. S. Kim, J. H. Moon, B. T. Lee, O. S. Song, and J. H. Je, J. Appl. Phys. **95**, 454 (2004).
[26] M. H. Kane, K. Shalini, C. J. Summers, R. Varatharajan, J. Nause, C. R. Vestal, Z. J. Zhang, and I. T. Ferguson, J. Appl. Phys. **97**, 023906 (2005).
[27] K. Masuko, A. Ashida, T. Yoshimura, and N. Fujimura, J. Appl. Phys. **103**, 043714 (2008).
[28] G. Lawes, A. S. Risbud, A. P. Ramirez, and R. Seshadri, Phys. Rev. B **71**, 045201 (2005).
[29] T. Fukumura, Z. W. Jin, M. Kawasaki, T. Shono, T. Hasegawa, S. Koshihara, and H. Koinuma, Appl. Phys. Lett. **78**, 958 (2001).
[30] S. Kolesnik, B. Dabrowski, and J. Mais, J. Appl. Phys. **95**, 2582 (2004).
[31] D. P. Joseph, G. S. Kumar, and C. Venkateswaran, Mater. Lett. **59**, 2720 (2005).
[32] C. Liu, F. Yun, and H. Morkoc, J. Mater. Sci.: Mater. Electron. **16**, 555 (2005).
[33] Y. Q. Chang, X. Y. Xu, X. H. Luo, C. P. Chen, and D. P. Yu, J. Cryst. Growth **264**, 232 (2004).
[34] K. P. Bhatti, S. Chaudhary, D. K. Pandya, and S. C. Kashyap, Solid State Commun. **140**, 23 (2006).
[35] J. Blasco, F. Bartolome, L. M. Garcia, and J. Garcia, J. Mater. Chem. **16**, 2282 (2006).
[36] H. J. Blythe, R. M. Ibrahim, G. A. Gehring, J. R. Neal, and A. M. Fox, J. Magn. Magn. Mater. **283**, 117 (2004).
[37] D. C. Kundaliya, S. B. Ogale, S. E. Lofland, S. Dhar, C. J. Metting, S. R. Shinde, Z. Ma, B. Varughese, K. V. Ramanujachary, L. Salamanca-Riba, and T. Venkatesan, Nature Mater. **3**, 709 (2004).
[38] K. Tanaka, K. Fukui, S. Murai, and K. Fujita, Appl. Phys. Lett. **89**, 052501 (2006).
[39] K. Tanaka, K. Fukui, S. Murai, and K. Fujita, J. Magn. Magn. Mater. **310**, 2095 (2007).
[40] J. Zhang, R. Skomski, and D. J. Sellmyer, J. Appl. Phys. **97**, 10D303 (2005).
[41] S. K. Mandal, A. K. Das, T. K. Nath, and D. Karmakar, Appl. Phys. Lett. **89**, 144105 (2006).
[42] C. H. Bates, W. B. White, and R. Roy, J. Inorg. Nucl. Chem. **28**, 397 (1966).
[43] K. R. Kittilstved and D. R. Gamelin, J. Appl. Phys. **99**, 08M112 (2006).
[44] K. R. Kittilstved and D. R. Gamelin, J. Am. Chem. Soc. **127**, 5292 (2005).
[45] J. M. D. Coey, M. Venkatesan, and C. B. Fitzgerald, Nature Mater. **4**, 173 (2005).
[46] B. Xiao, Z. Z. Ye, Y. Z. Zhang, Y. J. Zeng, L. P. Zhu, and B. H. Zhao, Appl. Surf. Sci. **253**, 895 (2006).
[47] S. W. Lim, M. C. Jeong, M. H. Ham, and J. M. Myoung, Jpn. J. Appl. Phys., Part 2 **43**, L280 (2004).
[48] S. M. Liu, S. L. Gu, J. D. Ye, S. M. Zhu, W. Liu, K. Tang, Z. P. Shan, R. Zhang, Y. D. Zheng, and X. W. Sun, Appl. Phys. A: Mater. Sci. Process. **91**, 535 (2008).
[49] D. J. Qiu, J. Wang, K. B. Ding, H. J. Shi, and Y. Jia, Acta Phys. Sin. **57**, 5249 (2008).
[50] H. Huhtinen, J. Raittila, P. Paturi, J. Salminen, and V. S. Zakhvalinskii, J. Phys.: Condens. Matter **14**, 7165 (2002).
[51] Y. J. Li, T. C. Kaspar, T. C. Droubay, A. G. Joly, P. Nachimuthu, Z. Zhu, V. Shutthanandan, and S. A. Chambers, J. Appl. Phys. **104**, 053711 (2008).
[52] L. A. Chick, L. R. Pederson, G. D. Maupin, J. L. Bates, L. E. Thomas, and G. J. Exarhos, Mater. Lett. **10**, 6 (1990).
[53] H. Pan, J. B. Yi, L. Shen, R. Q. Wu, J. H. Yang, J. Y. Lin, Y. P. Feng, J. Ding, L. H. Van, and J. H. Yin, Phys. Rev. Lett. **99**, 127201 (2007).

[54] N. S. Norberg, K. R. Kittilstved, J. E. Amonette, R. K. Kukkadapu, D. A. Schwartz, and D. R. Gamelin, J. Am. Chem. Soc. **126**, 9387 (2004).
[55] T. C. Kaspar, T. Droubay, V. Shutthanandan, S. M. Heald, C. M. Wang, D. E. McCready, S. Thevuthasan, J. D. Bryan, D. R. Gamelin, A. J. Kellock, M. F. Toney, X. Hong, C. H. Ahn, and S. A. Chambers, Phys. Rev. B **73**, 155327 (2006).
[56] J. Narayan, K. Dovidenko, A. K. Sharma, and S. Oktyabrsky, J. Appl. Phys. **84**, 2597 (1998).
[57] F. Farges, Phys. Rev. B **71**, 155109 (2005).
[58] A. Titov, X. Biquard, D. Halley, S. Kuroda, E. Bellet-Amalric, H. Mariette, J. Cibert, A. E. Merad, G. Merad, M. B. Kanoun, E. Kulatov, and Y. A. Uspenskii, Phys. Rev. B **72**, 115209 (2005).
[59] R. D. Shannon, Acta Crystallogr., Sect. A: Cryst. Phys., Diffr., Theor. Gen. Crystallogr. **32**, 751 (1976).
[60] J.-S. Kang, G. Kim, H. J. Lee, D. H. Kim, H. S. Kim, J. H. Shim, S. Lee, H. Lee, J.-Y. Kim, B. H. Kim, and B. I. Min, Phys. Rev. B **77**, 035121 (2008).
[61] R. E. Behringer, J. Chem. Phys. **29**, 537 (1958).
[62] T. C. Droubay, T. C. Kaspar, B. P. Kaspar, and S. A. Chambers, Phys. Rev. B **79**, 075324 (2009).
[63] J. K. Furdyna, J. Appl. Phys. **64**, R29 (1988).
[64] Y. Shapira, J. Appl. Phys. **67**, 5090 (1990).
[65] X. Gratens, V. Bindilatti, N. F. Oliveira, Y. Shapira, S. Foner, Z. Golacki, and T. E. Haas, Phys. Rev. B **69**, 125209 (2004).
[66] S. Kolesnik, B. Dabrowski, Z. Q. Wiren, H. Kepa, T. M. Giebultowicz, C. M. Brown, J. Leao, and J. K. Furdyna, J. Appl. Phys. **99**, 08M122 (2006).
[67] Y. Shapira and V. Bindilatti, J. Appl. Phys. **92**, 4155 (2002).
[68] B. W. Wessels, New J. Phys. **10**, 055008 (2008).
[69] K. Sato, H. Katayama-Yoshida, and P. H. Dederichs, Jpn. J. Appl. Phys., Part 2 **44**, L948 (2005).
[70] T. Fukushima, K. Sato, H. Katayama-Yoshida, and P. H. Dederichs, Jpn. J. Appl. Phys., Part 2 **45**, L416 (2006).
[71] S. Kuroda, N. Nishizawa, K. Takita, M. Mitome, Y. Bando, K. Osuch, and T. Dietl, Nature Mater. **6**, 440 (2007).
[72] M. A. White, S. T. Ochsenbein, and D. R. Gamelin, Chem. Mater. **20**, 7107 (2008).
[73] T. C. Kaspar, S. M. Heald, C. M. Wang, J. D. Bryan, T. Droubay, V. Shutthanandan, S. Thevuthasan, D. E. McCready, A. J. Kellock, D. R. Gamelin, and S. A. Chambers, Phys. Rev. Lett. **95**, 217203 (2005).
[74] X. F. Liu and R. H. Yu, J. Appl. Phys. **102**, 083917 (2007).
[75] P. V. Radovanovic and D. R. Gamelin, Phys. Rev. Lett. **91**, 157202 (2003).
[76] C. Song, S. N. Pan, X. J. Liu, X. W. Li, F. Zeng, W. S. Yan, B. He, and F. Pan, J. Phys.: Condens. Matter **19**, 176229 (2007).
[77] P. I. Archer, P. V. Radovanovic, S. M. Heald, and D. R. Gamelin, J. Am. Chem. Soc. **127**, 14479 (2005).
[78] J. D. Bryan, S. M. Heald, S. A. Chambers, and D. R. Gamelin, J. Am. Chem. Soc. **126**, 11640 (2004).
[79] T. C. Kaspar, T. Droubay, D. E. McCready, P. Nachimuthu, S. M. Heald, C. M. Wang, A. S. Lea, V. Shutthanandan, S. A. Chambers, and M. F. Toney, J. Vac. Sci. Technol. B **24**, 2012 (2006).
[80] T. C. Kaspar, T. Droubay, S. M. Heald, P. Nachimuthu, C. M. Wang, V. Shutthanandan, C. A. Johnson, D. R. Gamelin, and S. A. Chambers, New J. Phys. **10**, 055010 (2008).